Radiative Effects of Airborne Dust on Regional Energy Budgets at the Top of the Atmosphere

STEVEN A. ACKERMAN AND HYOSANG CHUNG

Cooperative Institute for Meteorological Satellite Studies, Space Science and Engineering Center, University of Wisconsin–Madison, Madison, Wisconsin

11 June 1990 and 22 July 1991

ABSTRACT

The effects of dust on the radiative energy budget at the top of the atmosphere were investigated using model calculations and measurements from the Earth Radiation Budget Experiment (ERBE). Estimates of the dust optical depth were made from observations of the Advanced Very High-Resolution Radiometer (AVHRR). Model calculations of the radiative fluxes at the top of the atmosphere were compared with ERBE measurements made during a dust outbreak that occurred over the Saudi Arabian peninsula during July 1985.

Measurements of the ERBE over the oceanic regions indicated that the presence of the dust increased the clear-sky shortwave radiative exitance (SWRE) at the top of the atmosphere (TOA) by 40–90 W m^{-2}. Over the desert regions the differences in the SWRE between clear and dust-laden regions were difficult to determine from the satellite observations. In contrast, the presence of dust over the ocean decreased the observed longwave radiative exitance (LWRE) at the TOA by 5–20 W m^{-2}, while over the desert regions its reduction was 20–50 W m^{-2}. The major discrepancy between the observations and calculations occurred for the SWRE over the desert.

1. Introduction

The geographic distribution of radiative energy is an important characteristic of a climate system and is determined by the incoming shortwave radiative energy, surface radiative characteristics, and the horizontal and vertical distribution of atmospheric constituents (e.g., water vapor, ozone, carbon dioxide, clouds, and aerosols). Dust, being a common aerosol over deserts (Takahashi and Arakawa 1981; Carlson and Prospero 1977; Carlson 1979), is an important regional climate variable. Dust can also be transported, over several days, from desert regions to nondesert regions (Prospero 1981; Reiff and Forbes 1986), and can therefore affect the climate of regions adjacent to deserts.

Several field experiments have documented the effects of dust on atmospheric heating rates and surface radiative energy budgets (Kondratyev et al. 1976; Carlson and Benjamin 1980; Cerf 1980; Ackerman and Cox 1982, 1987; Brinkman and McGregor 1983; Ellingson and Serafino 1984; Smith 1986; Fouquart et al. 1987). A variety of studies have used weather satellite observations in visible and infrared windows to locate and track dust outbreaks (Shenk and Curran 1974; Martin 1975; Ackerman 1989), infer dust mass loading (Wolfson and Matson 1986; Norton et al. 1980), and study the time and spatial variations of dust loading (Kondratyev et al. 1976; Rao et al. 1989). The detection of dust using visible channel imagery is most successful over oceanic regions because of the contrast produced by the dark ocean background. Over land, during the day, the presence of dust is better observed in the window infrared (10.5–12.5 μm) channel. The impact of dust on visible and infrared window channel radiances suggests that dust outbreaks may have a large impact on regional broadband radiative energy budgets.

This study employs shortwave and longwave two-stream adding models and satellite observations of the Earth Radiation Budget Experiment (ERBE) to study the effects of dust on the radiative fluxes at the top of the atmosphere. Section 2 discusses the models, their input variables, and results from simulations. Section 3 presents satellite analyses of the radiative impact of a dust outbreak observed over the Saudi Arabian peninsula in July 1985. This section also discusses the observations in relation to the theoretical calculations. The results of the study are summarized in section 4.

2. Radiative transfer calculations

Various mathematical methods have been developed to solve the radiative transfer equation (e.g., Irvine 1975; Lenoble 1977). This study uses two-stream adding models for both the shortwave and longwave spectrum to address the impact of dust on the radiation

Corresponding author address: Steven Ackerman, Cooperative Institute for Meteorological Satellite Studies, Space Science and Engineering Center, University of Wisconsin–Madison, 1225 W. Dayton St., Madison, WI 53706.

budget at the top of the atmosphere (TOA). Two-stream models consider only the upward and downward irradiances at a given level and are appropriate for computing radiative fluxes for a large range of atmospheric conditions (Meador and Weaver 1980; King and Harshvardhan 1986).

Several two-stream models for the shortwave (SW) spectral regime have been used in a variety of atmospheric studies (for review see Meador and Weaver 1980; King and Harshvardhan 1986). The SW two-stream model of the present study assigns layer reflectances and transmittances according to the hybrid model of Meador and Weaver (1980).

Two-stream multiple-scattering models have also been applied to the longwave (LW) radiative transfer equation (Schmetz and Raschke 1981; Stephens et al. 1990). This paper makes use of a LW two-stream model similar to that of Geleyn and Hollingsworth (1979) in which the Planck function $B(\tau)$ varies linearly with optical depth (Wiscombe 1976). The errors associated with this LW two-stream model are discussed in Ackerman and Cox (1987).

a. Model input parameters

The simulation of the radiative characteristics of a dust-laden atmosphere requires the following information: the thermodynamic structure of the atmosphere, the absorption and scattering properties of the air molecules, the absorption and scattering properties of the dust along with its vertical and horizontal distribution, the spectral reflectance and emittance of the surface, and the spectral distribution of extraterrestrial solar energy. These model input parameters will be discussed in this section. The present study focuses on the radiative characteristics of the dust overlying the Saudi Arabian peninsula and adjacent region and makes extensive use of the aircraft measurements of Ackerman and Cox (1982) and Patterson et al. (1983), as well as the surface measurements of Smith (1986). Similarity of the dust observed over Saudi Arabia with dust suspended over other geographic regions has been discussed by Ackerman and Cox (1988). The atmospheric temperature and moisture profiles are based on the observations of Ackerman and Cox (1982). It is not the intent of this paper to present a complete review of the single-scattering properties of dust, which was addressed by d'Almeida (1987) and Longtin et al. (1988). In this section, a brief description of the vertical and spectral variability of dust radiative characteristics observed over the Saudi Arabian region is presented as 1) a rationale for choosing the dust loadings discussed at the end of the section and 2) a comparison of model-determined radiative fluxes to aircraft observations.

The single-scattering properties of the aerosol are described in terms of the single-scattering albedo ω_0, the scattering phase function $P(\mu)$ [or the asymmetry parameter, $g = \frac{1}{2} \int P(\mu)\mu d\mu$], and the volume extinction coefficient, σ_{ext}. These parameters can be calculated (assuming spherical particles) from Mie theory given the aerosol index of refraction and the particle-size distribution. Differences between phase functions generated from Mie theory and those measured by a polar nephelometer for yellow sand observed over Japan have been discussed by Nakajima et al. (1989). Differences between Mie theory and observations of the phase functions for these large particles were primarily in the backward directions. This section makes use of the particle-size distributions measured over this region by Ackerman and Cox (1982) and the indices of refraction measured by Patterson et al. (1983). The spectral variation of single-scattering properties of soil-derived aerosols has been discussed by d'Almeida (1987), Longtin et al. (1988), and Ackerman and Cox (1988). Figure 1 depicts the vertical variation of ω_0 and g for six spectral intervals calculated from aircraft measurements at six different altitudes. Both ω_0 and g are constant with height, within the errors of the measured size distribution and index of refraction.

Figure 2 depicts the vertical structure of σ_{ext} over the Saudi Arabian peninsula determined from the measurements of Ackerman and Cox (1982) and Patterson et al. (1983). The measurements indicate a strong vertical variation of σ_{ext} with maximum values near the surface. This vertical variation is relatively independent of wavelength. Similarly, for high dust concentrations, Kashina (1965) found that the dust content of the surface layer varies exponentially with height, while DeLuisi et al. (1976) measured a highly variable vertical structure in aerosol concentration. Shaw (1980) measured a bimodal vertical structure in σ_{ext} in an Asian dust layer that was transported over the Hawaiian Islands; the primary peak occurred near the top of the layer, while the second smaller peak ex-

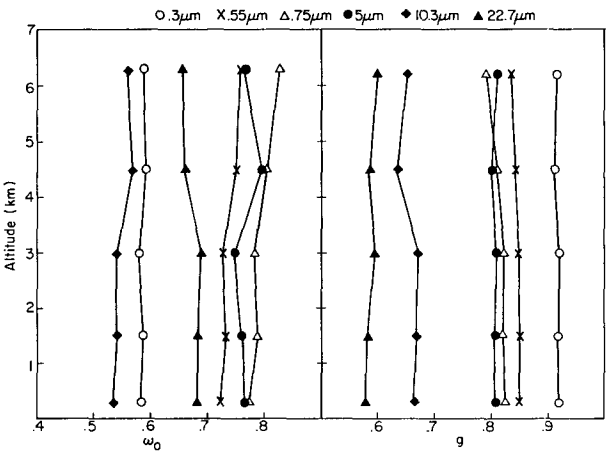

FIG. 1. Vertical variation of the single-scattering albedo and asymmetry parameter for six wavelengths, as determined by measurements made during SMONEX.

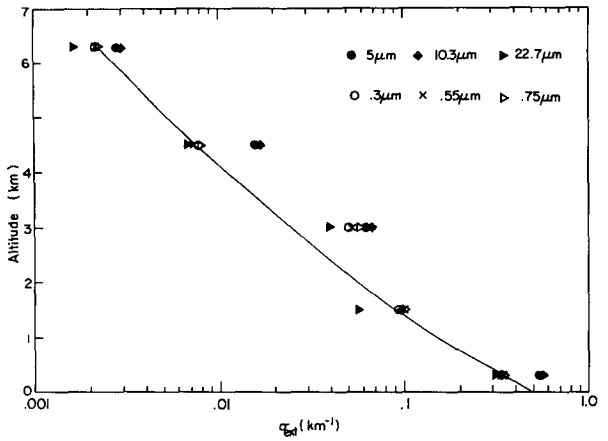

FIG. 2. Vertical variation of the extinction coefficient over the Saudi Arabian peninsula at six wavelengths, as determined from the measurements of Ackerman and Cox (1982) and Patterson et al. (1983).

isted at or just below the trade inversion and was attributed to the growth of hygroscopic particles. In their study of the radiative heating rates of Saharan dust, Carlson and Benjamin (1980) measured that σ_{ext} was nearly constant for their desert case, but used a vertical variation in σ_{ext} based on the measurements of Prospero and Carlson (1972) for their ocean case. Fouquart et al. (1987) assume that the normalized size distribution is independent of altitude.

Surface reflectivity is a function of surface composition and moisture content as well as the angular and spectral distribution of the incident radiation. This study assumes the desert surfaces to be dry; a wetting of the surface would decrease the surface albedo. Desert surfaces tend to display a distinct difference between visible and near-infrared albedos (Ackerman and Cox 1982; Smith 1986; Smith et al. 1980), with the latter being higher. The dependence of surface albedo on solar zenith angle also varies between the visible and near-infrared wavelengths. This study assumes the solar zenith angle dependence in the visible and near-infrared spectral regimes as measured by Smith (1986). Measurements by Coulson (1966) indicate that specular reflection from desert sand is small, and therefore, it is assumed that the reflected energy is entirely diffuse.

Emissivities integrated over the spectral region 8–12 μm for sandy soils generally vary between 0.9 and 0.98 (Gayevsky 1951; Buettner and Kern 1965). In the present study a surface emissivity of 0.95 is assumed for the LW window regime and a value of 1.0 is assumed for the remaining LW spectral intervals. An emissivity of 1.0 is assigned for water surfaces.

Molecular absorption is incorporated in the two-stream models by expressing the transmittance function averaged over the given spectral interval as a sum of exponentials (Wiscombe and Evans 1977). In the case of a layer in which both gases and aerosol are present, the layer-mean asymmetry parameter and the single-scattering albedo are weighted by their clear and dust optical depths. The scaling approximation discussed by Chou and Arking (1980) is employed to account for the nonhomogeneous water vapor pathlengths in the atmosphere. No pathlength correction is made for ozone.

The SW version of the two-stream adding model has 11 spectral bands: 6 water vapor absorption bands (0.94, 1.1, 1.38, 1.87, 2.7, and 3.2 μm) and 4 bands for the 0.2–0.8-μm spectral region. A solar constant of 1368 W m^{-2} is assumed and the energy distribution of each spectral interval is assigned according to the data of Thekaekara and Drummond (1971). The surface is assumed to be Lambertian. The longwave model consists of 20 spectral bands. The transmission of overlapping gases in the same spectral bandpass is discussed by Ohring and Joseph (1978).

b. Comparison of the doubling two-stream models and aircraft observations

In this section, the two-stream models discussed above are compared with aircraft radiative flux measurements made during the 1979 Summer Monsoon Experiment (SMONEX) as well as with a more accurate doubling adding model (Grant and Hunt 1969; Wiscombe 1976; Stephens 1978). The model input parameters are those discussed above, which are based on observations made over the Saudi Arabian peninsula. Aircraft flux observations are presented in Ackerman and Cox (1982).

Comparisons of model-calculated shortwave fluxes and aircraft-measured fluxes from two aircraft flights are depicted in Fig. 3. The solar zenith angle of the 10 May flight was 25.9°, while that of 12 May was approximately 75°. The surface albedos used in the model corresponded to either the visible (0.28–0.7 μm) or NIR (0.7–2.8 μm) albedo measured by the aircraft at it lowest altitude (approximately 0.3 km). In Fig. 3 the solid lines represent the upward or downward total SW fluxes, the dotted line represents the direct component of the downward flux, and the net SW flux is shown as the longer dashed line. The thick lines and the dotted line represent calculations made with the doubling model, while the thin lines depict the two-stream calculations. The *A*'s represent the aircraft-measured upward and downward fluxes (Ackerman and Cox 1982), while the *N*'s are the measured net fluxes. In general there is excellent agreement between the model and measured downward fluxes. Agreement is not as good for the upward fluxes and might be influenced by an incorrect specification of the surface boundary conditions, which vary considerably over the flight path (Smith et al. 1980). The two-stream model tends to overestimate the upward fluxes for the smaller zenith angle case, while it underestimates the flux for the large zenith angle case.

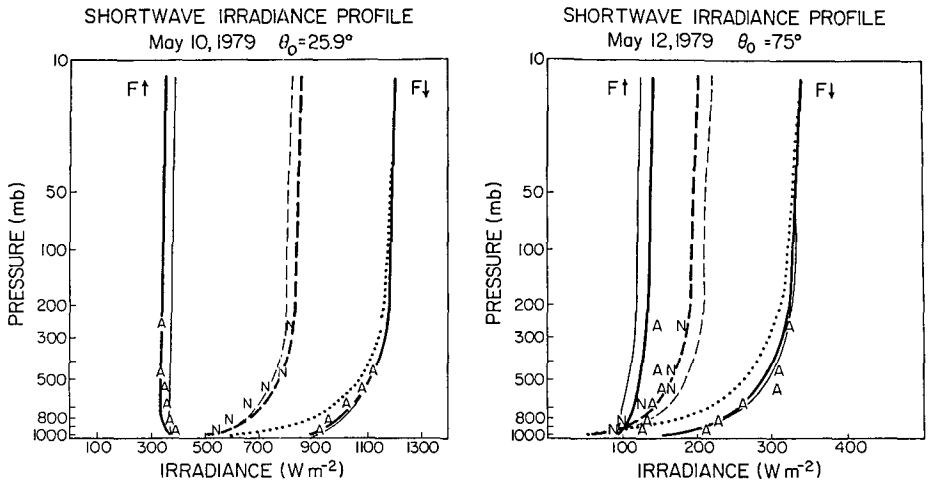

FIG. 3. Comparison of model-calculated shortwave fluxes to aircraft-measured fluxes made during the SMONEX over the Saudi Arabian peninsula. Solid lines represent the model-calculated upward or downward total SW fluxes, the dotted line represents the direct component of the downward flux, and the net SW flux is shown by the dashed line. The thick lines represent the calculations using the doubling model, while the thin lines depict the two-stream model results. The *A*'s represent the measured upward and downward fluxes, while the *N*'s are the measured net fluxes.

It is worthwhile to point out some of the interesting features of the model calculations. Solar absorption by the dust is large and occurs primarily in the visible portions of the spectrum. The presence of the dust layer not only reduces the total incoming flux, but also reapportions the energy between the direct and diffuse components. This redistribution is a strong function of the solar zenith angle. Within the dust layer the upward fluxes tend to decrease with height for the smaller solar zenith angle case and increase with height for the larger zenith angle case. In both cases the net flux and the downward flux increase with height.

Longwave flux comparisons of observations and the model calculations for a dust-laden atmosphere are shown in Fig. 4. Surface temperature was assigned according to aircraft measurements of a downward-facing spectral radiometer (Ackerman and Cox 1980) at the lowest flight altitude. Except for the downward fluxes at the lowest two aircraft flight levels, model calculations are generally within 4% of the measurements. Changing the size distribution or index of refraction does not substantially improve the agreement at the lowest two levels. Discrepancies between the model and observed fluxes are within the measurement errors of

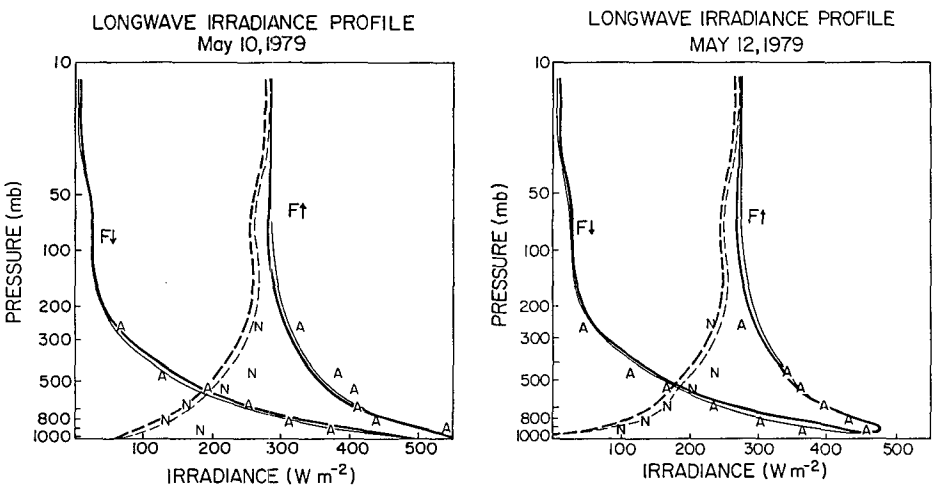

FIG. 4. Comparison of model-calculated longwave fluxes to aircraft-measured fluxes made during the SMONEX over the Saudi Arabian peninsula. Solid lines represent the model-calculated upward or downward total LW fluxes, and the net LW flux is shown as the dashed line. The thick lines represent the calculations using the doubling model, while the thin lines depict the two-stream model results. The *A*'s represent the measured upward and downward fluxes, while the *N*'s are the measured net fluxes.

the pyrgeometers. According to the model calculations, the dust primarily affects the 8–13-μm region. For example, the dusty–clear difference between the downward flux at the surface for the model atmosphere of 10 May is 61 W m^{-2}; of this difference, 56 W m^{-2} is accounted for in the 8–13-μm spectral interval.

c. Model results

The objective of this study is to assess the effects of dust on the radiative flux at the top of the atmosphere from model calculations and satellite observations. In order to reduce model biases, the effects are presented in terms of the differences between the model calculations for a dust-laden atmosphere and calculations for the same atmosphere with no dust. Aerosols scatter and absorb solar radiation, and as a result can cool or warm the earth–atmosphere system depending on the magnitudes of ω_0, g, the total dust loading, and the surface albedo and temperature. Large variations exist in the single-scattering properties of a dust layer, as discussed by d'Almeida (1987) and Longtin et al. (1988). Thus, representative dust-layer characteristics are chosen to quantify the changes in single-scattering properties, and thus the radiative fluxes. The index of refraction corresponds to that of Patterson et al. (1983) for the shortwave spectrum and Patterson (1981) for the longwave spectrum. Four different desert-layer microphysical characteristics were considered. These are:

DESERTL: This model assumes the microphysical properties of the dust layer to be constant with altitude with a size distribution corresponding to the light dust-loading distribution of Patterson and Gillette (1977). Thus, an increase in optical depth is attained by an increase in the number of particles. The top of the dust layer is located near 5 km with a base at the surface.

DESERTH: This case is similar to DESERTL with the exception that the dust particle size distribution corresponds to the heavy dust-loading case of Patterson and Gillette (1977). Thus, differences between DESERTL and DESERTH are in the single-scattering properties of the dust layer resulting from a change in size distribution.

DESERTV: The difference between DESERTV and the previous models is that this case allows for the vertical variation of σ_{ext} according to the observations of Ackerman and Cox (1982). The single-scattering albedo and asymmetry parameter are the same as in the DESERTL case.

OCEANL: The microphysical properties of the dust layer are assumed to be constant with altitude and reside within the 850–550-mb layer. The particle-size distribution corresponds to the light dust-loading distribution of Patterson and Gillette (1977).

Differences between the SW upward flux at the top of the atmosphere (TOA) for a dust-laden and dust-free environment of the DESERTL (solid) case are shown in Fig. 5 as a function of solar zenith angle and dust optical depth at 0.55 μm. The optical depth at a wavelength of 0.55 μm (τ_d) is used since this is the most common wavelength for inferring dust optical depths from surface measurements. Contour intervals are 20 W m^{-2}. Negative values indicate a greater upward flux for the clear-sky case; thus, the presence of the dust layer results in a net SW energy gain by the earth–atmosphere system. The largest changes resulting from increasing τ_d are for the smallest solar zenith angles, where the upward flux decreases due to absorption by the dust. Results for the DESERTH (dashed) and DESERTV (dotted) cases are also shown in Fig. 5. Changing the size distribution (DESERTL vs DESERTH) or the vertical structure of σ_{ext} (DESERTL vs DESERTV) results in differences of no more than approximately 15 W m^{-2}. The DESERTH case is "darker" than the DESERTL case due to the smaller single-scattering albedo and the larger asymmetry parameter. For $\tau_d < 1.2$ there is only a weak dependence on solar zenith angle for $\theta_0 < 40°$.

Dust-laden minus dust-free differences in the upward SW flux at the TOA for the OCEANL case are shown in Fig. 6. Contrary to the desert cases, dust over the low surface albedo of the ocean results in an increase in the upward flux with increasing turbidity, for a given solar zenith angle. Thus, the scattering processes dominate the absorption processes and the presence of the dust layer decreases the SW energy gain of the earth–

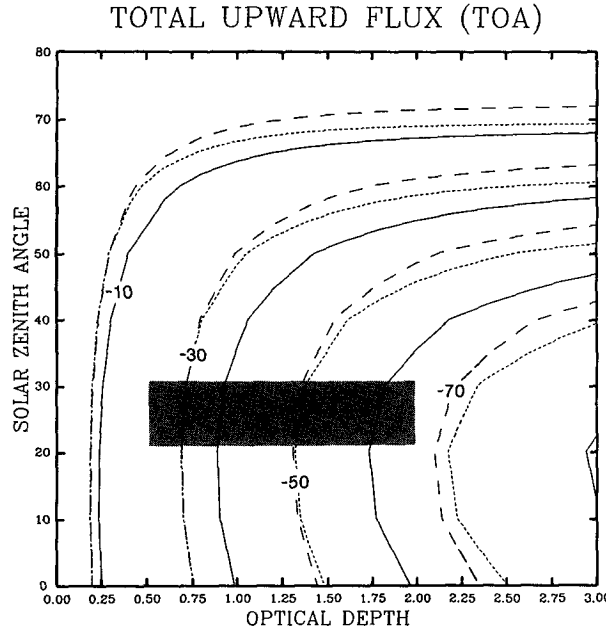

FIG. 5. Differences in the SW upward flux at the top of the atmosphere between a dust-laden and dust-free environment for the DESERTL (solid), DESERTH (long dashed), and DESERTV (short dashed) cases as a function of solar zenith angle and dust optical depth at 0.55 μm. Contour intervals are 20 W m^{-2}.

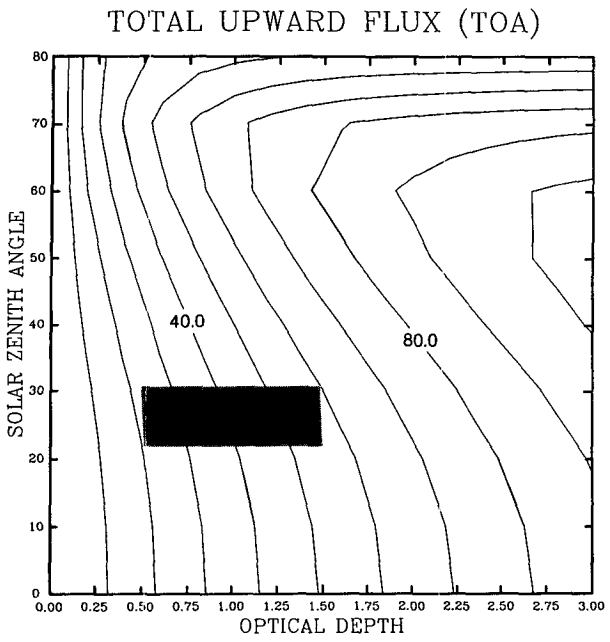

FIG. 6. Dust-laden and dust-free differences in the upward SW flux at the top of the atmosphere for the OCEANL case. Contour intervals are 10 W m^{-2}.

atmosphere system. In addition, the ocean case displays a greater sensitivity of the upward flux to changes in solar zenith angle and turbidity than the desert cases.

Differences in the LW flux at the TOA between clear-sky calculations and dusty atmosphere as a function of turbidity and surface temperature are shown in Fig. 7. Negative values indicate that the clear-sky values are greater than those for the dust-laden case. In studying the sensitivity of the LW fluxes to the presence of various dust-layer conditions, atmospheric temperatures above 850 mb are held fixed, based on observations of Ackerman and Cox (1982), while the temperature profiles from the surface to 850 mb vary diurnally. For surface temperatures less than approximately 25°C a temperature inversion exists. The DESERTL (solid) and DESERTH (dashed) cases are similar, showing decreases in the upward flux with increasing optical depth. This is due to the fact that the presence of the dust layer reduces the surface LW radiative energy losses to space, the impact being greater for higher surface temperatures. For the DESERTV case (dotted) where most of the dust is concentrated in the lowest atmospheric levels, the presence of the dust can lead to an increase in the TOA upward flux for lower surface temperatures and turbidities greater than about 0.4. This results from the lower-level temperature inversion in conjunction with the large dust concentrations near the surface.

3. Satellite observations

Dust is a relatively common phenomenon over the Arabian peninsula, with most dust outbreaks occurring during summer (Takahashi and Arakawa 1981; Ack-

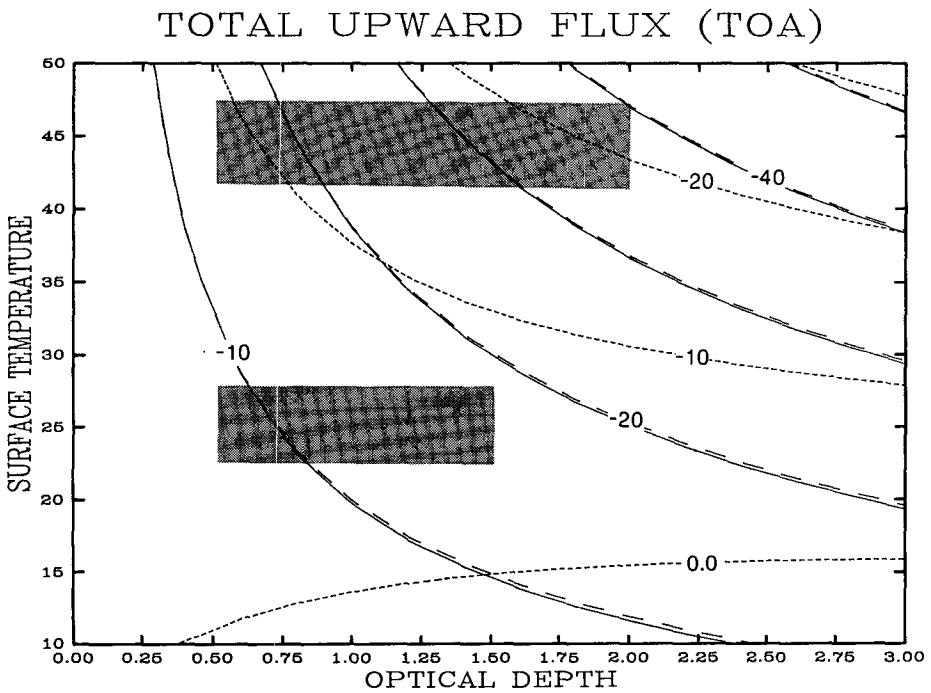

FIG. 7. Differences in the LW flux at the top of the atmosphere between a clear and a dusty atmosphere as a function of turbidity and surface temperature for the DESERTL (solid), DESERTH (dashed), and DESERTV (dotted) cases. Contour intervals are 10 W m^{-2}; negative values indicate a greater clear-sky value.

erman and Cox 1989). Meteosat imagery at 1200 UTC (ESA 1985) was employed as a means of surveying the presence of dust within the region 10°–40°N and 20°–60°E for the summer of 1985 (a year when ERBE data were available). Meteosat data have been used to locate and estimate the optical depth of dust over the Sahara (Jankowiak and Tanre 1988; Legrand et al. 1989). The thermal infrared (IR) window channel in the 10.5–12.5-μm spectral band was used to locate dust over land (Shenk and Curran 1974; Martin 1975). The visible channel (VIS) in the 0.4–1.1-μm spectral band was used to locate dust over the sea (Shenk and Curran 1974; Carlson 1979). The infrared water vapor channel (WV) in the 5.7–7.1-μm spectral band was used to discriminate cirrus clouds from dust clouds. Analyses of these Meteosat data (ESA 1985) revealed a dust outbreak that occurred over Saudi Arabia during the period 5–11 July 1985. This dust outbreak was verified from surface synoptic data archived by the National Center for Atmospheric Research and consists of four observations per day, nominally at 0000, 0600, 1200, and 1800 UTC.

NOAA-9 1.1-km resolution images of the AVHRR channel 1 (0.58–0.68 μm) and channel 4 (10.5–11.5 μm) observations made on 8 July are shown in Figs. 8a and 8b, respectively. On this day, the dust is seen over the Persian Gulf in the visible channel (Fig. 8a), spreading over the interior of the Arabian peninsula in the infrared image (Fig. 8b), and extending out over the Arabian Sea (Fig. 8a). The evolution of the dust outbreak, from analysis of satellite and surface observations, was similar to that discussed by Ackerman and Cox (1989); it began near Kuwait and moved east-southeast, engulfing the eastern and southern Arabian peninsula, the Persian Gulf, and the western Arabian Sea. This is the climatological pattern of dust movement for this region (Ackerman and Cox 1989).

Having located a dust outbreak, data from ERBE were used to study the effects of dust on the radiative energy budget (REB) at the top of the atmosphere. The ERBE archived data (Barkstrom et al. 1989) include observations of the solar constant, the reflected shortwave radiation, and the earth–atmosphere-emitted longwave radiation at the TOA. This study makes use of the ERBE scanner package (Kopia 1986) on board the *NOAA-9* polar-orbiting satellite. A complete discussion of the ERBE scanner is given by Kopia (1986). The inversion of satellite observations to TOA fluxes is discussed by Barkstrom et al. (1989).

The computation of the earth radiation budget from a scanning radiometer requires spectral and bidirectional models that are scene dependent. The ERBE inversion algorithms have five surface scene types (ocean, land, desert, snow, and coastal) combined with four cloud categories (clear, partly cloudy, mostly cloudy, and overcast). The geographic regions with dust will of course be misclassified, the majority of which are classified as partly and mostly cloudy. This misclassification will result in errors in the estimates of TOA fluxes. Errors resulting from assuming the wrong limbdarkening and bidirectional reflectance models due to incorrect scene identification have been studied by Dieckmann and Smith (1989). In that study it was demonstrated that the errors in the LW flux estimates were negligible for all scene types; maximum errors of the SW fluxes due to misclassification were 14%. Differences between the limb-darkening models of clouds and that of dust indicate that a misclassification will lead to an error of less than 5 W m^{-2}. For the SW fluxes we estimate, from the results of Dieckman and Smith (1989), that the misclassification of dust results in a maximum error of approximately 10%, or less than approximately 33 W m^{-2}.

To compare the ERBE observations discussed in the

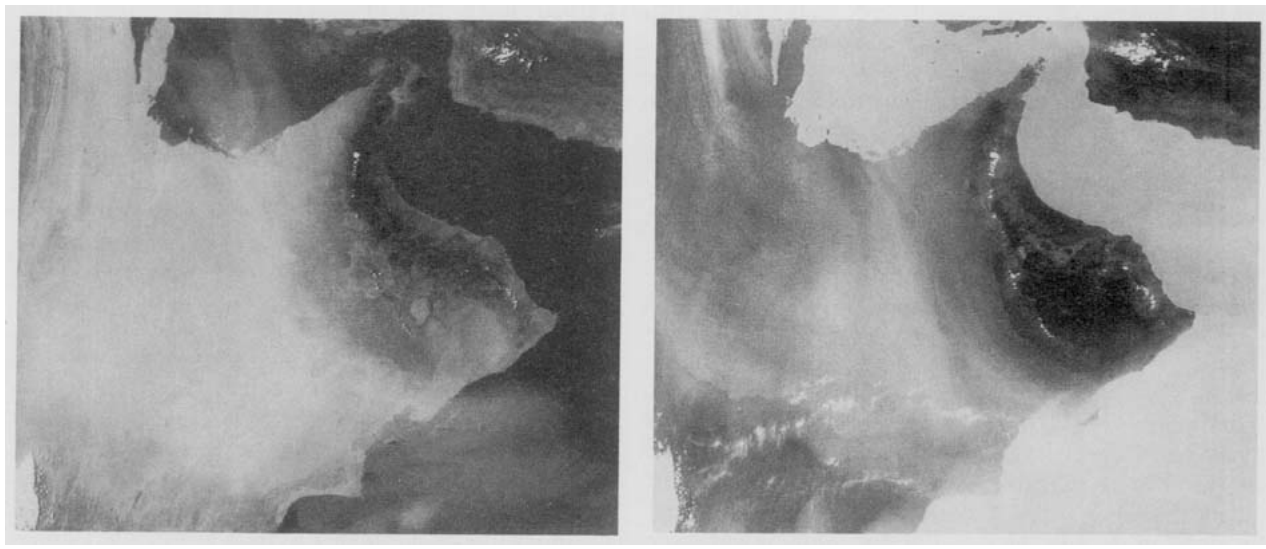

FIG. 8. *NOAA-9* AVHRR (a) channel 1 and (b) channel 4 observations on 8 July 1985.

next section with model calculations, an estimate of the dust loading is required. As direct measurements of the dust loading were not available, estimates must be made from the satellite observations. Rao et al. (1989) have presented a method of inferring aerosol optical thickness over oceans using radiances measured by the AVHRR channels 1 and 2. Application of this method to the observations over the Persian Gulf and Arabian Sea gives a range of optical thicknesses between 0.5 and 1.5.

The radiative temperature difference between the AVHRR 3.7- and 11-μm channels was investigated by Ackerman (1989) as a possible means of tracking dust outbreaks and estimating the dust-layer optical depth. Such an estimate could not be considered in this case as the AVHRR 3.7-μm channel begins to saturate due to the high surface temperatures associated with the interior desert, and the additional contribution from solar reflection. Carlson and Benjamin (1980) discuss the impact of dust on the infrared window channel temperatures. Observed differences between the AVHRR 11-μm temperatures between clear-sky conditions (either surrounding regions or values observed on 4 July) and dust-laden observations are approximately 5°–20°C. Comparing these differences with theoretical calculations indicates a range in total optical depths of 0.5–2.0, which is consistent with estimates over the ocean. This is not intended as an accurate assessment of the dust loading, but rather as an estimate to check the consistency between the ERBE observations and the theoretical calculations.

This range of optical depths deduced from satellite observations, as a function of the range in solar zenith angles and surface temperatures, is depicted in Figs. 5, 6, and 7 as shaded regions. The surface temperature ranges were estimated from AVHRR window and surface temperature observations over dust-free conditions. The range in the model-calculated differences between dust-laden and clear atmospheric TOA fluxes within these shaded regions will be compared to ERBE observations presented in the next section.

ERBE NOAA-9 scanner observations. Figures 9 and 10 depict, respectively, the shortwave (SWRE) and longwave (LWRE) radiative exitances at the TOA as measured from the *NOAA-9* for the time period 4–9 July 1985. Also shown in the figures are surface weather observations (S: dust; HZ: haze). On 4 July, while there are isolated observations of dust, there is no indication of a large-scale dust outbreak from the surface observations or from Meteosat imagery. The SWRE and LWRE over the Persian Gulf on 4 July are relatively constant at approximately 100 and 320 W m^{-2}, respectively. Over Saudi Arabia the LW fluxes range from approximately 330 to 355 W m^{-2}, while the SW fluxes vary from approximately 345 to 420 W m^{-2}.

The Meteosat and surface weather observations indicated that the dust outbreak began over northern Kuwait on 5 July. Due to the prevailing lower-layer northwesterlies over the Arabian peninsula, it is normal for the Arabian dust to head southeastward (Ackerman and Cox 1989). The effect of the dust on the REB at the TOA on 5 July can be seen as an area of minimum LW outgoing radiation near Kuwait, coincident with the dust outbreak region seen in the surface observations. The desert regions around the dust outbreak have LWRE fluxes ranging from 345 to 355 W m^{-2}, while those in the dust outbreak range from 310 to 335 W m^{-2}. The effect of the dust on the SW fluxes over land on 5 July is difficult to distinguish from the adjacent clear-sky region.

By 6 July the dust has spread eastward over the Persian Gulf and southward over the Arabian peninsula. Dust-free desert regions have LW fluxes ranging from 330 to 350 W m^{-2}, while nearby dust regions have LWRE fluxes from 300 to 320 W m^{-2}. A minimum in the LWRE over the interior of the peninsula (blue-green region) is due to high cirrus clouds, as seen in the Meteosat water vapor image. In the shortwave spectral region, the effects of the dust on the TOA fluxes are more distinctly seen over the northern end of the Persian Gulf, where there is an increase of 10–15 W m^{-2} due to the presence of the dust. The presence of dust decreases the clear-sky oceanic LWRE on 6 July by approximately 5–10 W m^{-2}.

By 7 July the dust has spread over most of the Arabian peninsula and has extended a substantial distance offshore, due to the continuation of the generally northwesterly flow of summer (Takahashi and Arakawa 1981; Ackerman and Cox 1989). Over the Arabian Sea the dust is seen in the SW as a band extending out from the coast of Oman. The dust increases the SWRE from approximately 100–110 W m^{-2} to 150–200 W m^{-2}, while the LWRE fluxes over the Arabian Sea decrease approximately 5–10 W m^{-2}. Over the desert, LWRE fluxes are 305–315 W m^{-2}, while clear desert regions are 340–350 W m^{-2}.

On 8 July, cloud and dust over the southern Arabian peninsula, Arabian Sea, and Indian Ocean are difficult to distinguish from one another in the ERBE broadband shortwave observations. An indication of the high cloudiness over these regions is made from Meteosat WV and AVHRR images and surface weather observations. Over the Arabian Sea off the coast of Oman, the dust increases the SWRE by approximately 70–90 W m^{-2}. The effects on the LW fluxes over the Arabian Sea are small, resulting in a decrease of approximately 5–10 W m^{-2}. Over the desert, the dust decreases the clear-sky LW TOA fluxes by approximately 30–45 W m^{-2}. By 9 July, the dust has engulfed the majority of the peninsula. The effect of the dust on the nighttime LW fluxes (not shown) during this period is less than 5 W m^{-2}.

In summary, a dust outbreak that occurred during July 1985 over the Saudi Arabian peninsula resulted in an increase in the SW TOA fluxes over the ocean of between 40 and 90 W m^{-2}. This observed increase is somewhat larger than the model-generated differences between dust-free and dust-laden conditions of

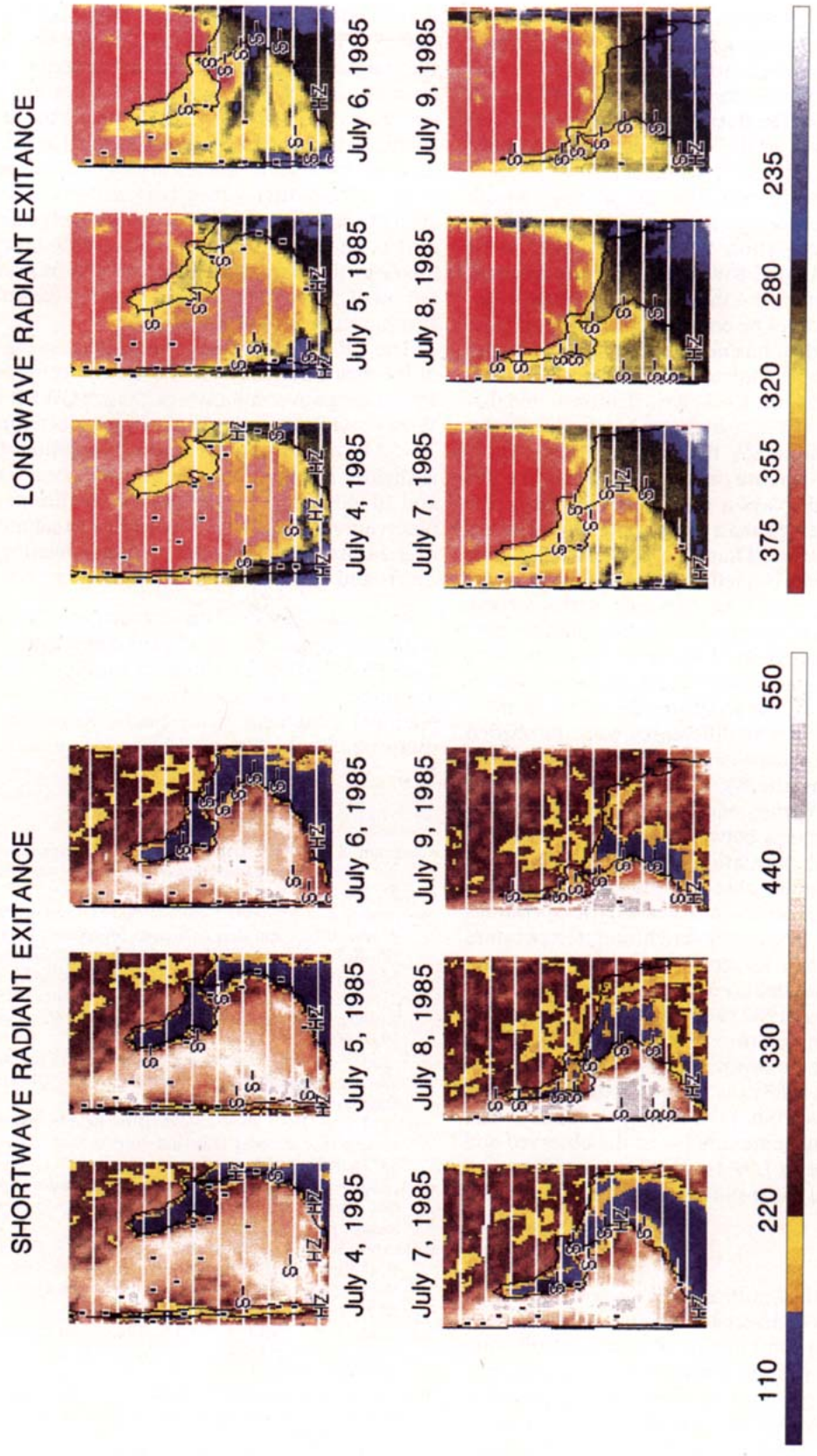

FIG. 9. Observations of the shortwave radiance exitance by the ERBE scanner on the *NOAA-9* for 4–9 July 1985. The color band at the bottom of the figure denotes the magnitude, in watts per square meter ($W\ m^{-2}$), of the *NOAA-9* observations.

FIG. 10. Observations of the longwave radiance exitance by the ERBE scanner on the *NOAA-9* for 4–9 July 1985. The color band at the bottom of the figure denotes the magnitude, in watts per square meter ($W\ m^{-2}$), of the *NOAA-9* observations.

approximately 20–60 W m^{-2}. Over the high-albedo desert regions the differences between SW TOA fluxes of the dust-free and dust-laden regions were difficult to determine in the observations. The theoretical calculations indicate a reduction in the outgoing SW flux due to absorption by the dust of approximately 20–60 W m^{-2}. Comparison of the model used in this study with aircraft observations indicates that the model is overestimating the upward SW flux at solar zenith angles of 25°, the average solar zenith angle of the *NOAA-9* overpasses. Thus, the discrepancy between observed and calculated SW fluxes over the desert is likely due to errors in the theoretical two-stream calculations. It should not be construed from the satellite observations that dust has no impact on the radiative budget of the desert. Carlson and Benjamin (1980) and Ackerman and Cox (1987) have demonstrated that dust increases the SW atmospheric heating while decreasing the incoming SW flux at the surface. These effects tend to compensate one another so that the SW flux at the TOA displays a smaller sensitivity to the dust optical properties than the surface fluxes or atmospheric absorption. Thus, the presence of a dust layer primarily results in a redistribution of the radiative energy between the atmosphere and the earth's surface.

From ERBE observations over the ocean, the presence of dust decreased the LW TOA fluxes by 5–20 W m^{-2}, while over the desert region the reduction in the LW TOA fluxes ranged from 20 to 50 W m^{-2}. Comparison of these LW differences with the shaded regions in Fig. 7 indicates a consistency between the ERBE observations, the AVHRR estimate of the dust loading, and the LW theoretical calculations. However, an inconsistency exists between the LW obervations and the theoretical calculations. The AVHRR 11-μm brightness temperature observations are less than the 12-μm (channel 5) equivalent blackbody temperatures by approximately 3°C. Such brightness temperature differences could not be reproduced with the single-scattering properties deduced from the observations of Ackerman and Cox (1982) and Patterson et al. (1983). The brightness temperature differences were also not reproducible using the composite desert aerosol models of Longtin et al. (1988), as the extinction coefficient generally increases from 11 to 12.5 μm. Thus, while there tends to be agreement between the observed and calculated broadband LW fluxes, there are discrepancies in the spectral distribution of energy.

4. Summary

The effects of a dust outbreak on the regional radiative energy budgets of desert and oceanic locations were investigated using a combination of model calculations and satellite observations. From the *NOAA-9* ERBE observations, the presence of the dust increased the SWRE at the TOA over the ocean by 40–90 W m^{-2}, but over the desert regions the differences were difficult to determine. Detection of the dust layer using the AVHRR SW channels was also difficult over the desert surface. Over the range of optical depths inferred from the AVHRR observations and the solar *NOAA-9* geometry, differences in the upward flux between clear-sky and dust-laden conditions for the ocean case ranged from 20 to 60 W m^{-2}, a slightly lower difference than the observations showed. In contrast, the model calculations for the desert cases indicate that the presence of dust decreased the clear-sky SWRE by 20–60 W m^{-2}. This discrepancy between observed and calculated SW fluxes over the desert is largely due to model errors. The small sensitivity of satellite-observed SW fluxes to the presence of dust results from a redistribution of the radiative energy between the atmosphere and the surface by the dust layer.

The ERBE observations indicate that the presence of the dust outbreak over the ocean decreased the observed longwave radiative exitance (LWRE) by 5–20 W m^{-2}, while over the desert regions its reduction was 20–50 W m^{-2}. From the model calculations this range is slightly smaller, 5–15 W m^{-2} for ocean conditions and 10–40 W m^{-2} for desert-type conditions. Both the observations and calculations indicate that the presence of the dust results in a net radiative heating over the desert and a net cooling over the ocean.

Acknowledgments. This research was funded by the National Aeronautics and Space Administration under Grant NAS1-18272. Computer support for analysis of the surface weather observations was provided by the National Center for Atmospheric Research, which is sponsored by the National Science Foundation.

REFERENCES

Ackerman, S. A., 1989: Using the radiative temperature difference at 3.7 and 11 μm to track dust outbreaks. *Remote Sens. Environ.*, **27**, 129–133.

——, and S. K. Cox, 1980: Colorado State University radiation instrumentation and data reduction procedures for the Convair 990 during Summer MONEX. Atmospheric Science Paper 325, 72, pp. [Colorado State Univ., Fort Collins, CO.]

——, and ——, 1982: The Saudi Arabian heat low: Aerosol distribution and thermodynamic structure. *J. Geophys. Res.*, **87**, 8991–9002.

——, and ——, 1987: Radiative characteristics of soil derived aerosols. Atmospheric Science Paper No. 417, 174 pp. [Colorado State University, Fort Collins, CO, 80523.]

——, and ——, 1988: Shortwave radiative parameterization of large atmospheric aerosols: Dust and water clouds. *J. Geophys. Res.*, **93**, 11 063–11 073.

——, and ——, 1989: Surface weather observations of atmospheric dust over the southwest summer monsoon region. *Meteor. and Atmos. Phys.*, **41**, 19–34.

Barkstrom, B. R., E. F. Harrison, G. L. Smith, R. Green, J. Kibler, R. D. Cess, and the ERBE Science Team, 1989: Earth Radiation Budget Experiment (ERBE): Archival and April 1985 results. *Bull. Amer. Meteor. Soc.*, **70**, 1254–1262.

Brinkman, A. W., and J. McGregor, 1983: Solar radiation in dense Saharan aerosol in Northern Nigeria. *Quart. J. Roy. Meteor. Soc.*, **109**, 831–847.

Buettner, K. J. K., and C. D. Kern, 1965: The determination of infrared emissivities of terrestrial surfaces. *J. Geophys. Res.*, **70**, 1329–1337.

Carlson, T. N., 1979: Atmospheric turbidity in Sahara dust outbreaks as determined by analyses of satellite brightness data. *Mon. Wea. Rev.*, **107**, 322–335.

——, and J. M. Prospero, 1977: Radiative characteristics of Sahara dust at solar wavelengths. *J. Geophys. Res.*, **82,** 3141–3152.
——, and S. G. Benjamin, 1980: Radiative heating rates for Saharan Dust. *J. Atmos. Sci.*, **37,** 193–213.
Cerf, A., 1980: Atmospheric turbidity over West Africa. *Cont. Atmos. Phys.*, **53,** 414–428.
Chou, M., and A. Arking, 1980: Computation of infrared cooling rates in the water vapor bands. *J. Atmos. Sci.*, **38,** 798–807.
Coulson, K. L., 1966: Effects of reflection properties of natural surfaces in aerial reconnaissance. *Appl. Opt.*, **5,** 905–917.
d'Almeida, G. A., 1987: On the variability of desert aerosol radiative characteristics. *J. Geophys. Res.*, **92,** 3017–3026.
DeLuisi, J. J., P. M. Furukawa, D. A. Gillette, B. G. Schuster, R. J. Carlson, W. M. Porch, R. W. Fegley, B. M. Herman, R. A. Rabinoff, J. T. Twitty, and J. A. Weinman, 1976: Results of a comprehensive atmospheric aerosol–radiation experiment in the southwestern United States. Part I: Size distribution, extinction optical depth and vertical profiles of aerosols suspended in the atmosphere. *J. Appl. Meteorol.*, **15,** 441–454.
Dieckmann, F. J., and G. L. Smith, 1989: Investigation of scene identification algorithms for radiation measurements. *J. Geophys. Res.*, **94,** 3395–3412.
Ellingson, R. G., and G. N. Serafino, 1984: Observations and calculations of aerosol heating over the Arabian Sea during MONEX. *J. Atmos. Sci.*, **41,** 575–589.
ESA, 1985: METEOSAT image bulletin. [European Space Operation Centre, Robert-Bosch-Str. 5, 6100 Darmstadt, Germany.]
Fouquart, Y., B. Bonnel, G. Brogniez, J. C. Buriez, L. Smith, and J. J. Moncrette, 1987: Observations of Saharan Aerosols: Results of ECLATS field experiment. Part II: Broadband radiative characteristics of the aerosols and vertical radiative flux divergence. *J. Climate Appl. Meteor.*, **26,** 38–52.
Gayevsky, V. L., 1951: Surface temperature of large territories. *Proc. Main Geophys. Obs.*, **1,** 291–310.
Geleyn, J. F., and A. Hollingsworth, 1979: An economical analytical method for the computation of the interaction between scattering and line absorption of radiation. *Contrib. Atmos. Phys.*, **52,** 1–16.
Grant, I. P., and G. E. Hunt, 1969: Discrete space theory of radiative transfer. I: Fundamentals. *Proc. Roy. Soc. Lond.*, **313,** 183–197.
Irvine, W. M., 1975: Multiple scattering in planetary atmospheres, *Icarus*, **25,** 175–204.
Jankowiak, I., and D. Tanre, 1988: Towards a climatology of the Saharan dust events over the Atlantic Ocean from METEOSAT imagery. *International Radiation Symp.*, Lille, France, Int. Assoc. Meteor. and Atm. Phys., 213.
Kashina, V. I., 1961: Dust content of the atmospheric surface layer in desert and semi-desert regions of central Asia and Kazakhstan. *Conf. on the Scattering and Polarization of Light in the Atmosphere.* Jerusalem, Israel Program for Scientific Translations, 1965.
King, M. D., and Harshvardhan, 1986: Comparative accuracy of selected multiple scattering approximations. *J. Atmos. Sci.*, **43,** 784–801.
Kondratyev, K. Y., O. D. Barteneva, L. I. Chapursky, A. P. Chernenko, V. S. Grishechkin, L. S. Ivlev, V. A. Ivanov, V. I. Korzov, V. B. Lipatov, M. A. Prokofyev, V. K. Tolkatchev, O. B. Vasiliev, and V. F. Zhvalev, 1976: Aerosol in the GATE area and its radiative properties. Atmospheric Science Paper No. 247, [Colorado State University, Fort Collins, CO 80523.]
Kopia, L. P., 1986: The Earth Radiation Budget Experiment scanner instrument. *Rev. Geophys.*, **24,** 400–406.
Legrand, M., J. J. Bertrand, M. Desbois, L. Menenger, and Y. Fouquart, 1989: The potential of infrared satellite data for the retrieval of Saharan dust optical depth over Africa. *J. Climate Appl. Meteor.*, **28,** 309–318.
Lenoble, J. (ed.), 1977: Standard procedures to compute atmospheric radiative transfer in scattering atmosphere. International Association of Meteorology and Atmospheric Physics. 125 pp. [National Center for Atmospheric Research, Boulder, CO 80307.]
Longtin, D. R., E. P. Shettle, J. R. Hummel, and J. D. Pryce, 1988: A wind dependent desert aerosol model: Radiative properties. AFGL-TR-88-0112.
Martin, D. W., 1975: Identification, tracking and sources of Saharan dust—an inquiry using Synchronous Meteorological Satellite (SMS). In WMO GATE Rep., **2,** 217–219.
Meador, W. E., and W. R. Weaver, 1980: Two stream approximations to radiative transfer in planetary atmospheres: A unified description of existing methods and a new improvement. *J. Atmos. Sci.*, **37,** 630–643.
Nakajima, T., M. Tanaka, M. Yamano, M. Shiobara, K. Arao, and Y. Nakanishi, 1989: Aerosol optical characteristics in the yellow sand events observed in May, 1982 at Nagasaki. Part II: Models. *J. Meteor. Soc. Japan*, **67,** 279–291.
Norton, C. C., F. R. Mosher, B. Hinton, D. W. Martin, D. Santek, and W. Kuhlow, 1980: A model for calculating desert aerosol turbidity over oceans from geostationary satellite data. *J. Appl. Meteor.*, **19,** 633–644.
Ohring, G., and J. H. Joseph, 1978: On the combined infrared cooling of two absorbing gases in the same spectral region. *J. Atmos. Sci.*, **35,** 317–322.
Patterson, E. M., 1981: Optical properties of the crustal aerosol: Relation to chemical and physical characteristics. *J. Geophys. Res.*, **86,** 3236–3246.
——, and D. A. Gillette, 1977: Commonalities in measured size distributions for aerosols having a soil-derived component. *J. Geophys. Res.*, **82,** 2074–2082.
——, G. W. Grams, and C. O. Pollard, 1983: Aircraft measurements of aerosol optical properties during the MONEX program. Final Technica Report, 28 pp.
Prospero, J. M., 1981: Arid regions as sources of mineral aerosols in the marine atmosphere. Special Paper No. 186, The Geological Society of America, 303 pp.
——, and T. N. Carlson, 1972: Dust concentration in the atmosphere of the equatorial North Atlantic Ocean. *J. Geophys. Res.*, **77,** 5255–5265.
Rao, C. R. N., L. L. Stowe, and E. P. McClain, 1989: Remote sensing of aerosols over the oceans using AVHRR data: Theory, practice and applications. *Int. J. Remote Sensing*, **10,** 743–749.
Reiff, J., and G. S. Forbes, 1986: African dust reaching northwestern Europe: A case study to verify trajectory calculations. *J. Climate and Appl. Meteor.*, **25,** 1543–1567.
Schmetz, J., and E. Raschke, 1981: An approximate computation of infrared radiative fluxes in a cloud atmosphere. *Pure Appl. Geophys.*, **119,** 248–258.
Shaw, G. E., 1980: Transport of Asian desert aerosol to the Hawaiian Islands. *J. Appl. Meteor.*, **19,** 1254–1259.
Shenk, W. E., and R. J. Curran, 1974: The detection of dust storms over land and water with satellite visible and infrared measurements. *Mon. Wea. Rev.*, **102,** 830–837.
Smith, E. A., 1986: The structure of the Arabian heat low. Part 1: Surface energy budget. *Mon. Wea. Rev.*, **114,** 1067–1083.
——, S. A. Ackerman, S. K. Cox, and T. H. Vonder Harr, 1980: Summer MONEX high altitude aircraft radiation measurements. [Department of Atmospheric Science, Colorado State University, Fort Collins, CO 50523.]
Stephens, G. L., 1978: Radiation profiles of extended water clouds, Part I: Theory *J. Atmos. Sci.*, **35,** 2111–2121.
——, S. Tsay, P. W. Stackhouse, and P. J. Flatau, 1990: The relevance of the microphysical and radiative properties of cirrus clouds to climate and climatic feedback. *J. Atmos. Sci.*, **47,** 1742–1753.
Takahashi, K., and H. Arakawa, 1981: Climates of Southern and Western Asia. *World Survey of Climatology, Vol.* **9,** H. E. Lansberg, Ed., Elsevier Scientific Publishing Company, 333 pp.
Thekaekara, M. P., and A. J. Drummond, 1971: Standard values of the solar constant and its spectral components. *Nature*, **229,** 6–9.
Wiscombe, W., 1976: Extension of the doubling method to inhomogeneous sources. *J. Quant. Spectrosc. Radiat. Transfer*, **16,** 477–489.
——, and J. W. Evans, 1977: Exponential-sum fitting of radiative transmission functions. *J. Comput. Phys.*, **24,** 416–444.
Wolfson, N., and M. Matson, 1986: Satellite observations of a phantom in the desert. *Weather*, **41,** 57–60.